Control of electron beam energy-spread by beam loading effects in a laser-plasma accelerator

OPEN ACCESS
Made open access 21 September 2020

IOP Publishing
Plasma Physics and Controlled Fusion

Plasma Phys. Control. Fusion **62** (2020) 055004 (10pp)
https://doi.org/10.1088/1361-6587/ab7c50

Control of electron beam energy-spread by beam loading effects in a laser-plasma accelerator

Guangyu Li[1], Quratul Ain[2,5], Song Li[3,5], Muhammad Saeed[1], Daniel Papp[3], Christos Kamperidis[3] and Nasr A M Hafz[3,4,5]

[1] Key Laboratory for Laser Plasmas (Ministry of Education), School of Physics and Astronomy, Shanghai Jiao Tong University, Shanghai 200240, People's Republic of China
[2] Department of Physics, University of Management and Technology, Lahore 54770, Pakistan
[3] ELI-ALPS, ELI-HU Non-Profit, Ltd., Dugonics tér 13, Szeged 6720, Hungary
[4] National Laboratory on High Power Laser and Physics, Shanghai Institute of Optics and Fine Mechanics, Chinese Academy of Sciences, Shanghai 201800, People's Republic of China

E-mail: ainnie357@yahoo.com, song.li@eli-alps.hu and nasr.hafiz@eli-alps.hu

Received 3 February 2020
Accepted for publication 3 March 2020
Published 23 March 2020

CrossMark

Abstract

We present experimental results from a laser wakefield electron accelerator driven by 70 TW ultrashort laser pulses in Helium and Helium–Nitrogen gaseous plasmas with two different Nitrogen concentrations, showing distinct electron-beam qualities. In order to get a clear view of the involved phenomenon, two-dimensional particle-in-cell simulations are performed which not only agreed with the experimental results but also provided an investigation on the evolution of accelerating structures. The experimental and simulation results depict that the beam loading effect can strongly modify the longitudinal accelerating electric field of the wake wave, imposing diametrically opposite effects on the final electron-beam qualities, especially the energy-spread, in the Helium–Nitrogen gas mixtures with different Nitrogen concentrations. In the Helium–Nitrogen-mixed plasma with a lower Nitrogen concentration (0.5%), if appropriately controlled, the beam loading effect can be employed to flatten the accelerating electric field for reducing the electron-beam energy spread. In contrast, in the Helium–Nitrogen-mixed plasmas with a higher Nitrogen concentration (5%), the accelerating electric field of the wake is locally reversed by the self-fields of the overloaded electron bunch, and the correspondingly generated negative-slope region of electric field increases the electron-beam energy-spread.

Keywords: laser wakefield acceleration, ionization injection, experimental laser plasma acceleration

(Some figures may appear in colour only in the online journal)

1. Introduction

Laser wakefield electron acceleration (LWFA), which was first observed in particle-in-cell simulations (PIC) by Tajima and Dawson in 1979 [1], has the potential to be the basis of a non-conventional technology for building ultra-compact, next-generation high-energy accelerators because of its capability of providing accelerating fields more than three orders of magnitude higher than achievable in conventional RF-based particle accelerators [2–5]. When an ultra-short ultra-intense laser pulse propagates through an optically transparent plasma, the radial pondermotive force of the laser pulse drives a spherical plasma wake by expelling plasma electrons from its path. In this bubble (or blowout) regime [6], the large associated accelerating field goes beyond several hundreds of GV m^{-1}. If the background plasma electrons are injected [7, 8] into the correct phase of the wakefield, they can be accelerated to high energies,

[5] Authors to whom any correspondence should be addressed.

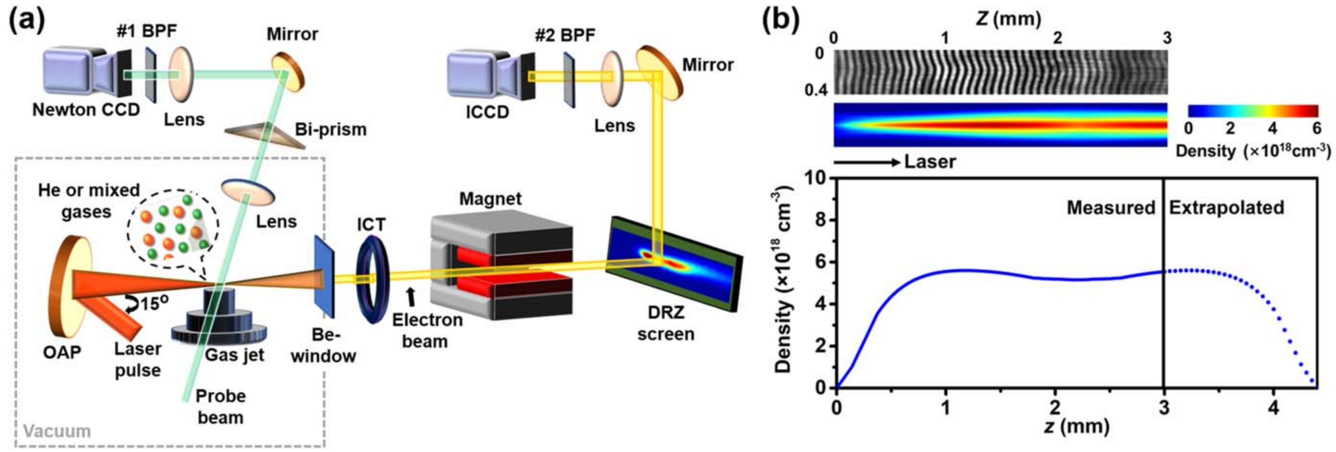

Figure 1. (a) Experimental setup for a LWFA driven by 70 TW laser pulses in Helium gas and Helium–Nitrogen mixed gases of different Nitrogen concentrations. Details are given in the text and BPF represents bandpass filters with different central wavelengths 800 and 546 nm for #1 and #2, respectively. (b) An interferogram for the electron density measurement and the corresponding 2D distribution and on-axis profile of the electron density for fully ionized plasma generated by the interaction of intense laser pulse with the mixed gas of 0.5% Nitrogen + 99.5% Helium.

generating collimated and quasi-mono-energetic electron beams. To overcome the non-linear evolution of the laser pulse and the challenge to generate stable and reproducible electron beams via the electron self-injection or spontaneous injection into the plasma wave, several injection mechanisms have been tested to control the electron injection such as optical injection [9–11], bubble evolution [12], and density-ramp injection [13–15]. A simple, yet effective electron injection scheme, which is known as ionization injection and requires a lower laser-intensity threshold as compared to that for triggering the self-injection, was proposed in 2008 and was recently demonstrated [16–19]. This scheme utilizes the ionization of inner-shell electrons of high-*Z* gas atoms (like Nitrogen, Oxygen, Argon, Krypton, etc), which are mixed with low-*Z* gas atoms (such as Helium which was used for the current study), near or at the peak intensity of laser pulse. The leading part of the laser pulse pre-ionizes the background low-*Z* gas atoms (e.g., Helium) completely along with the outer-shell ionization of high-*Z* gas atoms (e.g., Nitrogen), to form the plasma wake wave. The inner-shell electrons of high-*Z* gas atoms slip backward relative to the plasma wake when they are ionized at the peak of the laser pulse intensity. They are then trapped by the wake wave and gain enough energy via longitudinal acceleration. However, an electron beam generated by this scheme typically has a large energy spread due to continuous ionization and trapping of the inner-shell electrons throughout the whole length of the mixed plasma or up to the depletion of the laser pulse. Later, this scheme was revisited by introducing the 'self-truncated ionization injection (STII)' version in 2014 [20–22], where the electron injection length could be shortened to a few hundred micrometers, much shorter than the mechanical limits achieved so far. The initiated unmatched laser pulse ($k_p w_0 \neq 2\sqrt{a_0}$) truncates the injection process due to violation of the ionization injection condition ($\Delta\psi \geqslant 0.9$, where $\Delta\psi = \Delta\psi_{\rm ion} - \Delta\psi_{\rm btm}$ is the potential difference between the electron ionization and trapping positions of the first wake wave [20, 22]) because the self-focusing process leads to a very strong evolution of the wakefield and deforms the bubble before the end of the mixed plasma. After that, an additional improvement of the STII scheme [23] was proposed by employing the beam loading effects [24–26], and it enabled loading of charges of ~0.5 nC within a mono-energetic peak [23].

The doping concentration of the high-*Z* gas in the low-*Z* gas has a direct influence not only on the injection mechanism but also on the quality of the generated electron beam. Lower concentrations, typically less than 1% of the Nitrogen gas was used for the STII and resulted in electron beams with narrow energy spreads, as shown in [22, 27]. Our recent experimental work showed that higher concentrations (5% and 10%) of Nitrogen (or Krypton) gas lead to a dramatic degradation in the energy spectra of the electron beams [28–30]. However, the detailed investigation to explain the various physical mechanisms related to the doped concentration of the trace gas has not been explored so far. The current study provides a detailed microscopic perspective on the distinctions of LWFA in the mixed gases of Helium and Nitrogen of different Nitrogen concentrations. It has been observed that, in case of low concentration (0.5%) of the Nitrogen gas, the STII of two *K*-shell Nitrogen electrons dominates the injection process, and then the appropriately controlled beam loading effect further suppresses the final energy spread of accelerated electron beam; while in case of high concentrations (5%) of the Nitrogen gas, the ionization injection is activated at an early stage and rapidly terminated due to an over-loading of the injected electrons, which locally reverses the accelerating electric field of the wake wave to further increase the final electron-beam energy-spread in the following acceleration. Quantitative analysis via two-dimensional (2D) particle-in-cell (PIC) simulations is performed along with the experimental results.

2. Experimental setup

Figure 1(a) schematically shows the experimental setup for generating electron beams via the LWFA scheme using 70 TW, horizontally (*p*-) polarized, 800 nm laser pulses with 30 fs pulse duration. Laser pulses were focused on the front edge of a 4 mm long (along the laser propagating direction) slit-shaped supersonic gas jet [31–33] via an off-axis parabolic mirror (OAP) having a 200 cm focal length (*F* number is 20). The measured laser focal spot had a 25 μm radius of $1/e^2$ Gaussian intensity distribution. The peak laser intensity I_L and corresponding normalized vector potential a_0 were around 6×10^{18} W cm^{-2} and 1.7, respectively. The laser pulses were focused 2 mm above the gas jet to create an underdense plasma which was online probed using a 6 mJ laser pulse, which was split-off the main pulse after the laser compressor, via interferometric techniques [34]. After crossing the plasma perpendicular to the main beam direction, the probe beam generated interferogram via a Fresnel bi-prism which was then imaged by a 16 bit CCD camera. Electron density with a trapezoidal profile of 1 mm linear entrance and exit ramps and 2 mm plateau at $(5.4 \pm 0.2)\times10^{18}$ cm^{-3} was obtained by utilizing Abel inversion and 2D fast Fourier transformation (FFT) techniques on the interferograms, as shown in figure 1(b). A beryllium (Be) window was used to couple the electron beam from the vacuum chamber into the diagnostic system installed in air. A calibrated integrating current transformer (ICT) [35] was used for monitoring the electron-beam charge. An 8 cm×16 cm dipole magnet having 2 cm gap between the poles and an effective magnetic-field intensity of 1 T was used as an electron beam energy spectrometer. A Gd_2O_2S:Tb fluorescent (DRZ) screen monitored by a 16 bit intensified CCD (ICCD) camera was placed at 26.5 cm away from the magnet entrance to obtain the dispersed electron beam with electron energies above 60 MeV. The resolutions of this home-built energy spectrometer were $\pm2.5\%$ and $\pm5\%$ at 150 MeV and 300 MeV, respectively.

3. Experimental results

Figure 2 shows a series of energy spectra and the corresponding total charge of the electron beams generated from the LWFA in pure Helium and in mixtures of Helium and Nitrogen gaseous plasmas with different concentrations of 0.5% and 5% Nitrogen, respectively. Except for the concentration difference, all other parameters are kept constant during the experiment. Figure 2(a) shows a multiple of typical electron energy spectra produced by the LWFA in Helium plasma via self-injection into the plasma wave, which exhibits unstable characteristics with respect to energy and charge. In figure 2(a), shots #1, #2, and #5 show quasi-monoenergetic electron beams having broad relative energy spreads (14%–45%), moderate charges (22–87 pC), and an average full-width-at-half-maximum (FWHM) angular divergence of 3.7 mrad, whereas shots #3 and #4 shows monoenergetic electron beams having narrower relative energy spreads

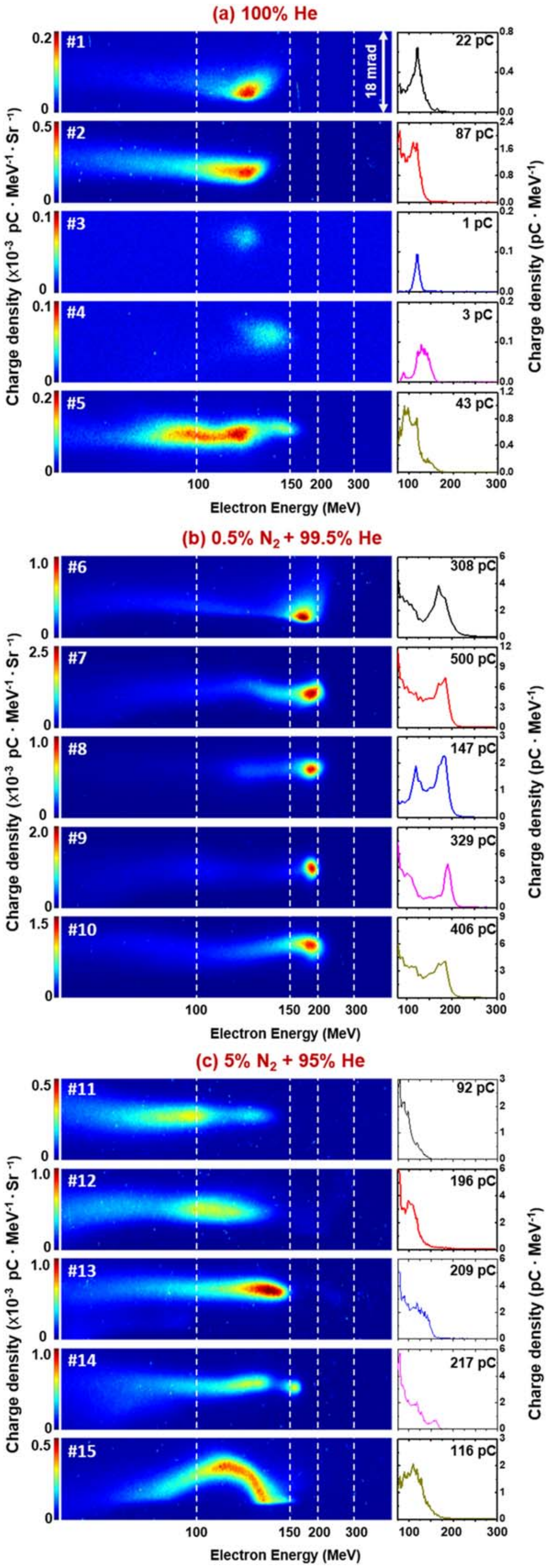

Figure 2. Typical energy spectra of electron beams and corresponding lineouts obtained from the LWFA in three different gaseous plasmas at the same electron density of $5.4 \pm 0.2 \times 10^{18}$ cm^{-3}. (a) Helium; (b) 0.5% Nitrogen mixed with 99.5% Helium; (c) 5% Nitrogen mixed with 95% Helium.

(9% and 23%, respectively), nominal charges (1 pC and 3 pC, respectively), an average angular divergence of 3.5 mrad, and the particular characteristic of no dark-current background.

On the other hand and for the case of LWFA in 0.5% Nitrogen +99.5% Helium plasma, multiple electron energy spectra are shown in figure 2(b). The energy spectra show that the STII mechanism is the main contributor to the electron injection process in this case , which results in narrow-energy-spread electron beams. Both of the STII conditions [22] are fulfilled in this case, namely, the Helium gas is doped with a very small fraction (0.5%) of Nitrogen whose *K*-shell electrons are fully ionized and subsequently trapped only near the peak intensity of the laser pulse, and the laser-plasma parameters for the current experiment are unmatched, i.e. $k_{\mathrm{p}}w_0 = 6.2 > 2\sqrt{a_0} = 2.7$. Due to self-focusing of laser pulse and the evolution of wakefield, the injection of electrons is restricted in time, limiting the energy spread. The obtained maximum peak energy is close to 200 MeV and the maximum charge is 500 pC, as shown in shots #7 of figure 2(b). Shot #9 in figure 2(b) also shows a high-quality monoenergetic beam, which has the narrowest relative energy spread of only 3%, a high charge of 329 pC, and a FWHM angular divergence of 3 mrad. It is clear that there is a common characteristic among those five electron energy spectra, i.e. most of the beam charge is concentrated in the mono-energetic peak.

When the Nitrogen concentration increases to 5%, the electron beam quality remarkably decreases, as shown in figure 2(c). Compared with the electron beams generated from the LWFA in the mixed gases of 0.5% Nitrogen + 99.5% Helium, the peak energies and relative energy spreads of the accelerated electron beams clearly degrade when mixed gases of 5% Nitrogen + 95% Helium are used. The maximum peak energy obtained is around 154 MeV in a two-bunch spectrum as shown in shot #14 of figure 2(c), where the high-energy bunch has a narrow relative energy spread of 4% and the low-energy bunch has a broad spectrum with another relative energy spread of 23% and a FWHM angular divergence of 3 mrad. Those results show the same trends in terms of energy spectra as our previous works [22, 27–30]. However, what is different from our previous work is that there is a remarkable decrease on the total charges of electron beams measured by the ICT from the mixed gases of 5% Nitrogen + 95% Helium as compared with those electron beams from the mixed gas of 0.5% Nitrogen + 99.5% Helium. This may be due to the fact that a lot of ionization-injected electrons from Nitrogen atoms could not be accelerated to high energies and they were lost during the propagation to the ICT.

4. 2D-PIC simulations and discussion

To understand and compare the detailed processes of electron beam acceleration in the above three different cases, 2D-PIC simulations were conducted using OSIRIS 4.0 framework with a moving window scheme [36]. In the simulations, all the laser and plasma parameters were kept as close as possible to the experimental parameters. That is, 800 nm *p*-polarized laser pulses with a power of 70 TW, laser focal spot w_0 of 25 μm, and normalized vector potential a_0 of 1.7, were focused at 1 mm inside 4 mm long gas targets. The gas densities had a trapezoidal profile extended from $z = 0$ to 4 mm (1 mm linear entrance and exit ramps and 2 mm plateau), and the gas densities of plateau were set at 3.2×10^{18} cm^{-3} and 2.75×10^{18} cm^{-3} for Helium and Helium–Nitrogen-mixed gases, respectively. The simulation box, which moves at the speed of light, was 120×160 μm^2 in size and was divided into cells with size of 0.015625×0.25 μm^2. Each simulation cell contained 14 particles inside. Overall mixed gas densities are the same for the two different Nitrogen concentration cases, i.e. 0.5% and 5% Nitrogen in Helium, except the amount of the doped neutral gas. In the simulations, the ionization of neutral Helium and Nitrogen gases was modeled in based on the Ammosov–Delone–Krainov tunnel ionization model [37]. We specified the maximum number of ionization levels of Helium and Nitrogen to be 2 and 7 respectively, and the ionization rate for each ionization level was defined and given in [38].

In figure 3, the upper-half panels show the longitudinal electric field, the laser fields and the corresponding density distributions of the He^{2+} electrons in *x*–*z* computational plane for different positions of the acceleration process in the Helium gas at the gas density of 3.2×10^{18} cm^{-3}. In case of Helium gas, we performed multiple simulations using gas densities of 2.75×10^{18}, 3×10^{18}, 3.1×10^{18}, 3.2×10^{18}, and 3.3×10^{18} cm^{-3}, respectively. It is found that, for the current laser pulse conditions, 3×10^{18} cm^{-3} is the threshold gas density for triggering self-injection and acceleration of the He^{2+} electrons. However, at the gas densities of 3×10^{18} cm^{-3} and 3.1×10^{18} cm^{-3}, self-injection of He^{2+} electrons occurs at a very late time (typically, after laser propagation of 3.5 mm), generating electron beams with low energy of <50 MeV. When the gas density was increased to 3.3×10^{18} cm^{-3}, the final electron beam energy reached 250 MeV, which does not agree with our experimental results presented in figure 2(a). The lower-half panels of figure 3 show the corresponding electron distributions in phase space and lineouts of the injected electrons' energy spectra at different stages of LWFA. From figures 3(a) and (b), one can see that there is no injection occurred in the first half length of the Helium gas target; the trailing second and third wake bubbles evolve faster than the first wake bubble, leading to the primary occurrence of self-injection of He^{2+} electrons in the second wake bubble [39] after a propagation distance of ~3 mm. Meanwhile, few electrons inside the second bubble are accelerated to an energy of approximately 100 MeV, as shown in figure 3(c). After 3.5 mm of propagation (see figure 3(d)), more electrons are injected into the second bubble, however, the acceleration of these electrons has been terminated with a maximum energy of ~100 MeV because of the disappearance of the second bubble; additionally, tiny amounts of electrons are injected into the first wake bubble but the deformation of the first bubble also limits the acceleration of those electrons to a maximum energy of ~120 MeV. Finally, an electron beam having a continuous energy spectrum up to ~150 MeV is generated from the

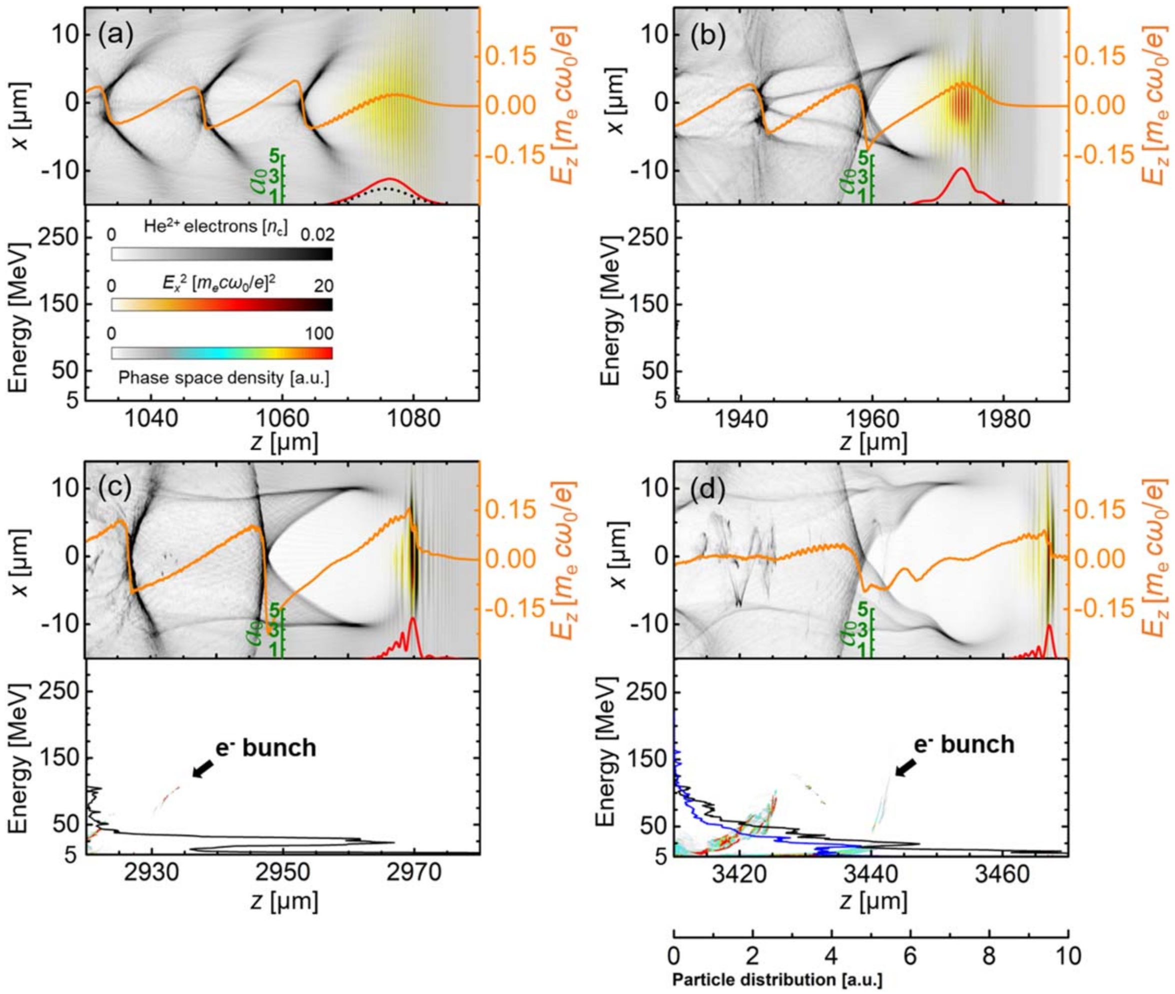

Figure 3. Snapshots for the evolution of the LWFA in *Helium* at the atomic gas density of 3.2×10^{18} cm^{-3}. The upper-half panels show the laser fields and the density distributions of the He^{2+} electrons in x–z plane. The lower-half panels show the phase-space distributions and energy spectra of the injected and accelerated electrons. Black dotted line in (a) shows the initial laser intensity along the laser axis, and the red lineouts (in the upper-half panels) correspond to a_0 showing the evolution of the laser intensity profile along the propagation direction, respectively. The orange lines in the upper-half panels are longitudinal electric field (wakefield) E_z along the laser axis. The blue line in (d) shows the electron beam's final energy spectra after a propagation distance of 4 mm.

LWFA in Helium plasma, as shown in the blue line in figure 3(d), which is in consistence with the experimental result of shot #5 presented in figure 2(a).

In figure 4, the upper-half panels in (a)–(e) show the longitudinal electric fields along with the laser fields and the corresponding density distributions of the background-plasma electrons (the He^{2+} electrons and the L-shell N$^{(1-5)+}$ electrons) and the injected electrons (only the K-shell N$^{6+,7+}$ electrons) respectively, in x–z computational plane at different positions of the LWFA acceleration process in the 0.5% Nitrogen + 99.5% Helium gas mixture at the gas density of 2.75×10^{18} cm^{-3}. Since such a gas density is lower than the threshold for triggering the He^{2+} electrons as mentioned above, the self-injection of He^{2+} electrons was not observed over the entire interaction length, as shown in figure 4. The lineouts of the laser intensity profile in terms of a_0 can be also seen in the upper-half panels. The lower-half panels in (a)–(e) show the corresponding electron distributions in phase-space and lineouts of the injected electrons' energy spectra. A very small number of the K-shell N$^{6+,7+}$ electrons are ionization-injected into the first bubble of the wake at ∼1.06 mm, which is just at the beginning of the plateau region of the gas density profile, as shown in figure 4(a). It is clear that at this early position of LWFA, figure 4(a), the peak value of a_0 has just reached ≈3 due to self-focusing, which is lower than the value of 3.8 required for self-trapping of electrons into the first bubble of the wake in the blowout regime as demonstrated by previous simulations [40] and an overview of many experiments [41]. Thus, it is also proved that self-injection of electrons into the first bubble of the wake wave cannot occur. Only ionization-induced injection in the first bubble continues for several hundred micrometers and then self-truncates, as shown in figure 4(b). Simultaneously, due to the beam loading effect, these injected electrons partially flatten the longitudinal accelerating electric field [23] near the center of first bubble and is kept nearly constant until the end of the plasma medium, as shown in figures 4(b)–(e). In the tailored longitudinal accelerating electric field, the field near the end of the bubble is obviously higher than that near its center, resulting in a stronger acceleration for the late-trapped

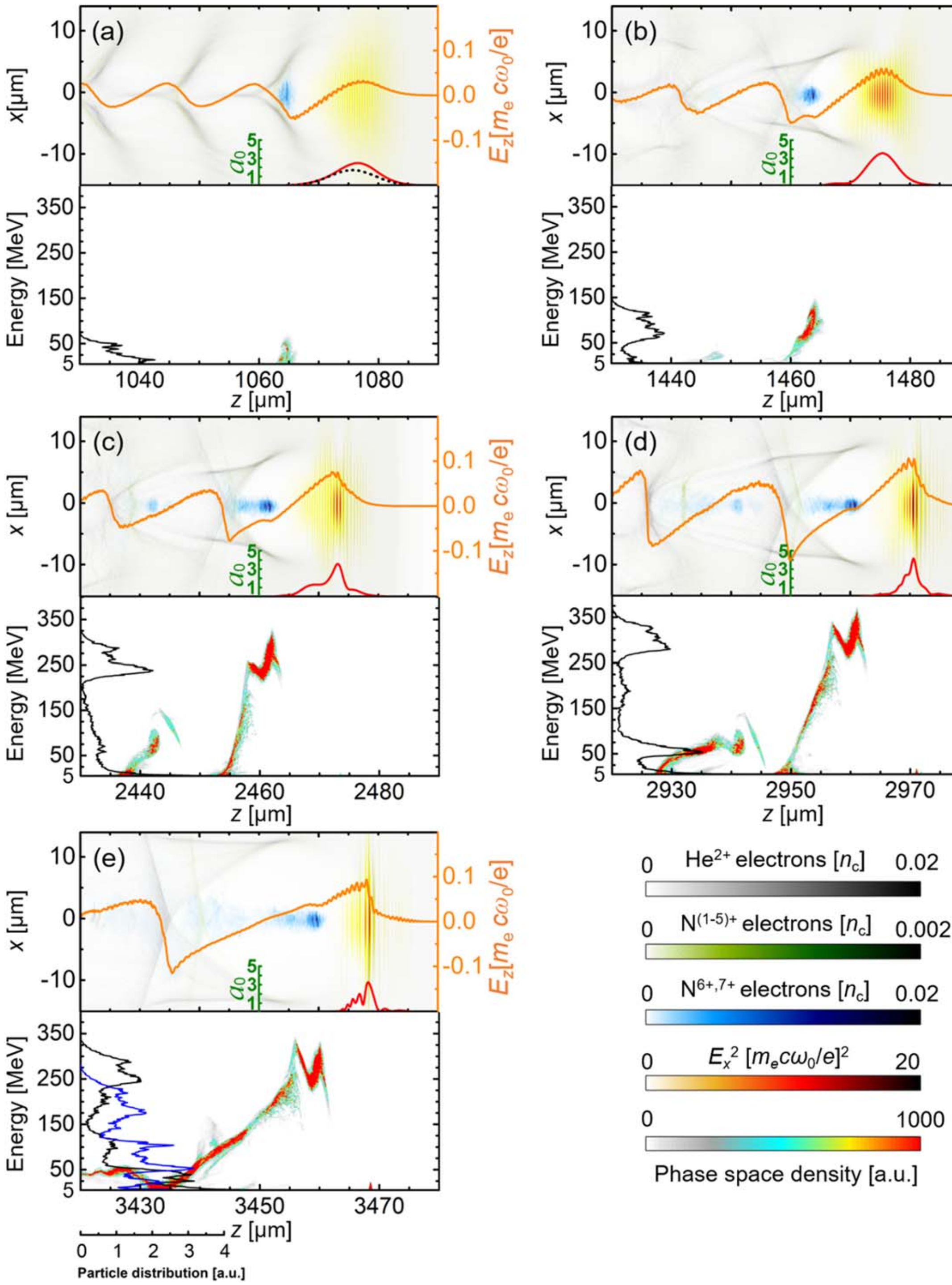

Figure 4. Snapshots for the evolution of the LWFA in the gas mixture of *0.5% Nitrogen + 99.5 Helium* at the atomic gas density of 2.75×10^{18} cm^{-3}. The upper-half panels show the laser fields and the density distributions of the He^{2+} electrons (gray-scale), the *L*-shell $N^{(1-5)+}$ electrons (green-scale), and the *K*-shell $N^{6+,7+}$ electrons (blue-scale) in *x*–*z* plane. The lower-half panels show the phase-space distributions and the energy spectra of the injected and accelerated electrons. Black dotted line in (a) shows the initial laser intensity along the laser axis, and the red lineouts (in the upper-half panels) correspond to a_0 showing the evolution of the laser intensity profile along the propagation direction, respectively. The orange lines in the upper-half panels show the longitudinal electric field (wakefield) E_z along the laser axis. The blue graph in (e) shows the electron beam's final energy spectra after a propagation distance of 4 mm.

low-energy electrons as compared with the acceleration experienced by the early trapped high-energy electrons. Thus, we can see that the energy spread of the accelerated quasi-monoenergetic electron beam is reduced gradually in the remaining acceleration process, as shown by the phase-space distributions of the injected electron beam in figures 4(c) and (d). Similar phenomenon of 'wakefield engineering' has been exploited in numerical simulations of electron-beam-driven plasma wakefield accelerator (PWFA) [42]. After a propagation distance of ∼3 mm, the leading quasi-monoenergetic electron bunch with the reduced energy spread enters into the decelerating phase of wake, as shown in figure 4(e). Finally, the energy spectrum of electron beam with a relatively narrow energy spread at acceleration distance of 4 mm is obtained, as shown in figure 4(e) in blue line, which agrees with the experimental results of figure 2(b). In addition, a subsequent ionization injection of a small number of the two *K*-shell $N^{6+,7+}$ electrons in the second bubble is observed at the distance ~2.44 mm, as shown in figures 4(c)−(e). However, such a second electron bunch could not obtain a significant high energy acceleration, contributing a background noise to the final quasi-monoenergetic energy spectrum of the electron beam, as shown in figure 4(e).

On the other hand, figure 5 shows the evolution of the LWFA in the gas mixture of 5% Nitrogen + 95% Helium at the gas density of 2.75×10^{18} cm^{-3}. There is obviously a large number of Nitrogen *K*-shell electrons trapped in both the first and second bubbles of the wakefield at the beginning of the laser-plasma interaction, as shown in figure 5(a), which differs from the LWFA in 0.5% Nitrogen + 99.5% Helium, figure 4. After that, only a small number of these electrons injected into the first bubble are sufficiently accelerated to 100 MeV, whereas majority of these electrons (mainly injected into the second bubble) are accelerated to very low-energy around < 5 MeV; simultaneously, the ionization injection of electrons in the first bubble also truncates, as shown in figure 5(b). Due to the higher electron charge over-loaded in the first bubble, the now pronounced beam loading effect has a significant impact on the longitudinal electric field used for acceleration, generating a negative-slope region in it near the center of bubble. The early-trapped electrons with high energies, which are located in the negative-slope region, further obtain a stronger acceleration than the later-trapped electrons with low energies. Therefore, one can see that the energy spread of accelerated quasi-monoenergetic electron beam in the first bubble further increases gradually in the remaining acceleration process, as shown in the phase-space distributions of the injected electrons in figures 5(c) and (d). Similarly, the two electron bunches injected into the first bubble enter the decelerating phase after a propagation distance of ~3 mm, as shown in figure 5(e). In the second bubble of the wakefield, the ionization injection of two *K*-shell $N^{6+,7+}$ electrons lasts until the end of the mixed plasma of 5% Nitrogen + 95% Helium, as shown in figure 5. Due to the relatively weak accelerating electric field and the mis-matching in phase with it, those injected electrons in the second bubble did not receive significant acceleration from the wakefield, contributing to generation of a low-energy tail (<50 MeV) in the spectrum of electron beam. Additionally, according to the phase-space distributions of the injected electrons, one can see that the total number of injected electrons with energies >5 MeV in the simulation in this case of mixed gas of 5% Nitrogen + 95% Helium are remarkably lower than those in the simulation of the 0.5% Nitrogen + 99.5% Helium gas case. This result agrees well with the decrease of the experimentally measured beam charge by the ICT (see figure 2) from the LWFA in the gas mixture of 5% Nitrogen + 95% Helium as well. Ultimately, an electron beam having a lower energy up to 150 MeV, larger energy spread, and relatively lower charge is generated in this case, as shown in the blue line in figure 5(e), which is consistent with the experimental results in figure 2(c).

Figure 6(a) shows the evolution of the laser peak intensity (a_0) in the LWFA in Helium gas at the gas density of 3.2×10^{18}cm^{-3} and the gas mixtures of 0.5% Nitrogen + 99.5% Helium and 5% Nitrogen + 95% Helium at the gas density of 2.75×10^{18}cm^{-3}, respectively. It is seen that the laser peak intensity experiences self-focusing and defocusing and its evolution in the Helium gas case is faster than that in the other cases, due to relatively high gas density. The value of a_0 evolved in the Helium gas reaches 4 after a propagation distance of ~2.5 mm, meaning that the self-injection could be triggered after this propagation distance at the gas density of 3.2×10^{18} cm^{-3}, as discussed in figure 3. The values of a_0 evolved in the other two cases and reached 4 after a propagation distance of ~3 mm and then quickly dropped below 4 again. It means that the self-injection (electrons from the Helium) might be triggered at ~3 mm and then immediately truncated within a short distance, leading to a negligible contribution from the Helium electrons to the total injected charge as compared with the ionization injection which is dominant. Figure 6(a) also shows the wake wave pseudo-potential difference ($\Delta\psi$) between the Nitrogen's *K*-shell electron ionization position ($\Delta\psi_{\rm ion}$) and the end of the first wake wave ($\Delta\psi_{\rm btm}$) for the two gas mixture cases, where the dotted blue and red lines represent results from the 0.5% Nitrogen + 99.5% Helium and 5% Nitrogen + 95% Helium, respectively. One can see that gradually the laser intensity is above the ionization threshold for the Nitrogen's *K*-shell (which requires $E_{\max} > 1.9$) as it is strongly self-focused in both two cases. The ionized *K*-shell electrons ($N^{6+,7+}$ electrons) can be trapped only if they gain enough energy from the wake, which needs $\Delta\psi \geqslant \Delta\psi_{\rm th} = 1 - \gamma_0^{-1}\sqrt{(1 + p^2/m_e^2c^2)} = 0.9$ [20, 22, 43], where the normalized transverse momentum p is estimated to be the normalized laser vector at the ionization position, i.e. $p = 1.9$, and the Lorentz factor γ_0 of the wake phase velocity at the gas density of 2.75×10^{18} cm^{-3} is estimated by the linear theory $\gamma_0 = \omega/\omega_{\rm p} = 18$, as the dotted black line shown in figure 6(a). The ionization-injection process takes place within a limited region in space (from 700 to 1000 μm) for the two mixed gas cases in the first half of the plasma medium. Correspondingly, figure 6(b) shows the total injected electron beam charge as a function of the laser propagation distance from the simulations for the two mixed gas cases. One can notice that the ionization injection of electrons has both occurred after ~0.7 mm of laser propagation and the injected beam charge saturates almost over the same laser propagation distance, which is around 1.5 mm. However, the mechanism of the truncation of ionization injection is rather distinct for the two cases. For the LWFA in 0.5% Nitrogen + 99.5% Helium, the ionization injection of *K*-shell Nitrogen electrons is self-truncated at ~1.5 mm due to the breakdown of ionization-injection condition ($\Delta\psi \geqslant 0.9$), where about 16 pC μm^{-1} of charge in 2D slab geometry (or

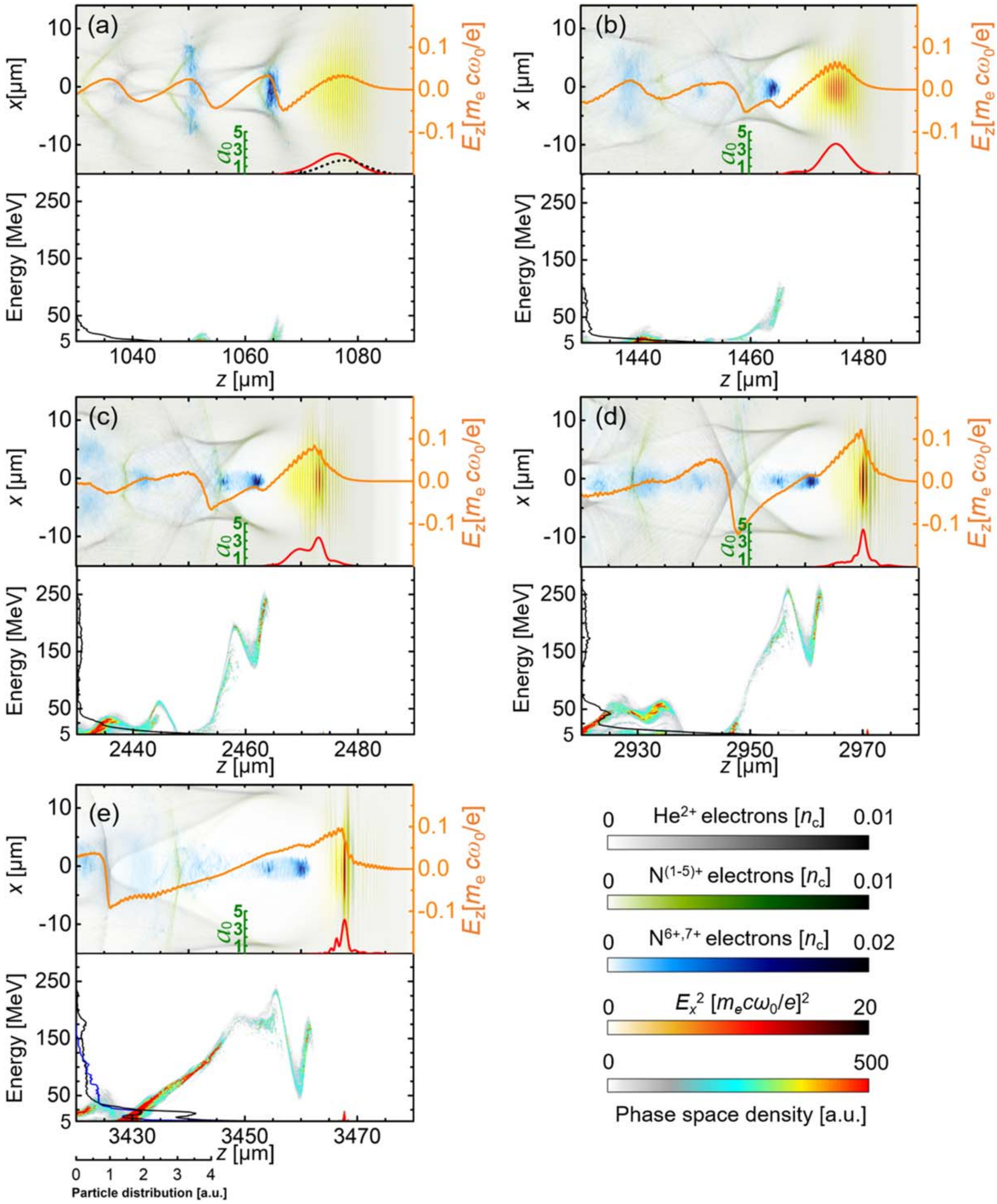

Figure 5. Snapshots for the evolution of the LWFA in the gas mixture of *5% Nitrogen + 95% Helium* at the atomic gas density of 2.75×10^{18} cm^{-3}. The description of the details of each panel in this figure is similar to those of figure 4.

112 pC if we assume the width of the beam is 7 μm, which is a common beam width) is injected into the wake wave. After that, the growth trend of the injected charge has slowed down significantly and eventually saturated at about 55 pC μm^{-1}, meaning that there is an additional ionization injection of *K*-shell Nitrogen electrons in the second bubble of wakefield which contributes to the low-energy tail of the electron energy spectrum, as consistent with the result in figure 4(e). For the LWFA in the 5% Nitrogen + 95% Helium, not only the injection rate of electrons is much faster, but also the total injected charge is much higher than those in the other case, and the ionization-injection process has been terminated at the distance of ~1.5 mm as well, where the total injected charge reaches 83 pC μm^{-1}. According to the equation of maximum affordable number of electrons in the bubble regime, i.e. $N \simeq 2.5 \times 10^9(\lambda[\mu\text{m}]/0.8) \times \sqrt{P[\text{TW}]/100}$ [8], the beam loading should occur when the charge approaches 335 pC (or 48 pC μm^{-1} of charge in 2D slab geometry if we assume the width of the beam is 7 μm as well). Thereafter, it can be inferred that the ionization injection has been truncated at the

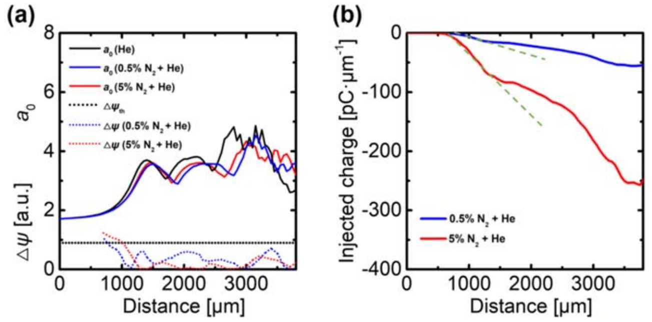

Figure 6. (a) Evolution of the laser peak intensities (a_0) for the LWFA in Helium gas at the gas density of 3.2×10^{18} cm^{-3} and the two cases of Helium–Nitrogen gas mixtures at the gas density of 2.75×10^{18} cm^{-3} and evolution of the pseudo-potential differences ($\triangle\psi$) for the two LWFA in the Helium–Nitrogen gas mixtures at the same gas density. The laser peak intensities are normalized to $E_{\rm laser} = m_e c\omega_L e^{-1} = 4 \times 10^{12}$ V m^{-1}. a.u., arbitrary units.
(b) Injected electron number or charge as a function of the laser propagation distance for the two gas mixture cases at the gas density of 2.75×10^{18} cm^{-3}. The dash green lines are linear fittings for the data with propagation distance from 700 to 1500 μm. The charge unit is pC μm^{-1} in the 2D slab geometry.

distance of ~1.5 mm due to the beam loading effect in the LWFA of 5% Nitrogen +95% Helium. Similarly, there is also an additional injection during the distance range of around 2.5–3.5 mm because of the ionization injection of Nitrogen electrons in the second bubble of the wakefield as seen in figure 5, and the whole injection process finally terminates at the level of ~250 pC μm^{-1}.

If we make a comparison between the present experimental and simulation results and our previous works [22, 27–30], several notable differences are found. Firstly, although the laser power has been nearly doubled in the present experiment, the electron-beam energies have not been remarkably increased or even decreased compared with those obtained by using the mixed gases of 0.3% Nitrogen + 99.7% Helium [27], 0.5% Nitrogen + 99.5% Helium [22, 28, 29], and 0.5% Krypton + 99.5% Helium [30] in our earlier work; this is related to a degradation of laser focusing quality in the current experiment. Secondly, PIC simulations in our previous works mainly focused on the control of final electron-beam energy and energy spread by manipulating the injection process of electrons [22, 28] and the effect of Nitrogen concentration on the divergence angle (or emittance) of electron beam [28, 29]. However, the time evolution of the accelerating structure during the whole LWFA in the Helium–Nitrogen-mixed gases are investigated in a great detail by the PIC simulations in the current work, and it is found that the beam loading effect plays an important role in controlling the final electron-beam energy spread by appropriately manipulating the Nitrogen concentration. Finally, mono-energetic electron beams with very high charge of ~0.5 nC are generated from the LWFA in the mixed gas of 0.5% Nitrogen + 99.5% Helium in the current experiment, which is in good agreement with the previous results [23].

5. Conclusion

In summary, we present experimental results from a laser wakefield acceleration in Helium gas and mixtures of Helium–Nitrogen gases with low (0.5%) and high (5%) concentrations of Nitrogen, showing very different electron-beam qualities. 2D-PIC simulations are performed to support the experimental results and provide a microscopic view of different mechanisms which influence the injection and acceleration of the electron beams. The STII scheme dominates electron injection of the LWFA and the beam loading effect subsequently suppresses the energy spread of the injected electron bunch in the plasma of 0.5% Nitrogen + 99.5% Helium, resulting in monoenergetic beams with narrow energy spreads. On the contrary, the LWFA in the plasma of 5% Nitrogen+95% Helium, abundant *K*-shell Nitrogen electrons are ionized and trapped in the wake wave, leading to beam over-loading which terminates the ionization-injection process and further increases the energy spread of the injected electron bunch by locally reversing the accelerating electric field which leads to generation of low-quality beams in this case. These results can be considered as a reference for the future applications of LWFA-based electron beams or x-ray sources.

Acknowledgments

This work was partially supported by the National Basic Research Program of China (Grant No. 2013CBA01500). This work was partially supported by the ELI-ALPS project (GINOP-2.3.6-15-2015-00001) which is supported by the European Union and co-financed by the European Regional Development Fund. N A M H acknowledges President's International Fellowship Initiative (PIFI) of Chinese Academy of Sciences (CAS); International Partnership Program (181231KYSB20170022) of CAS; Inter-Governmental Science and Technology Cooperation of Chinese Ministry of Science and Technology (MOST). We are grateful to the OSIRIS Consortium at UCLA and IST for providing access to the OSIRIS 4.0 framework. Simulations were conducted on the PI supercomputer at the Center for High Performance Computing at SJTU.

ORCID iDs

Guangyu Li https://orcid.org/0000-0003-1373-7303
Quratul Ain https://orcid.org/0000-0002-1496-9547
Song Li https://orcid.org/0000-0002-5974-1140
Nasr A M Hafz https://orcid.org/0000-0003-4371-5551

References

[1] Tajima T and Dawson J M 1979 *Phys. Rev. Lett.* **43** 267
[2] Hafz N A M *et al* 2008 *Nat. Photon.* **2** 571
[3] Leemans W *et al* 2014 *Phys. Rev. Lett.* **113** 245002

[4] Gonsalves A J *et al* 2019 *Phys. Rev. Lett.* **122** 084801
[5] Li S *et al* 2019 *Sci. Adv.* **5** eaav7940
[6] Pukhov A and Meyer-ter-Vehn J 2002 *Appl. Phys.* B **74** 355
[7] Lu W *et al* 2006 *Phys. Rev. Lett.* **96** 165002
[8] Lu W *et al* 2007 *Phys. Rev. ST Accel. Beams* **10** 061301
[9] Rechatin C *et al* 2009 *Phys. Rev. Lett.* **102** 164801
[10] Faure J *et al* 2006 *Nature* **444** 737
[11] Esarey E *et al* 1997 *Phys. Rev. Lett.* **79** 2682
[12] Zeng M *et al* 2012 *J. Plasma Phys.* **78** 363
[13] Geddes C G R *et al* 2008 *Phys. Rev. Lett.* **100** 215004
[14] Gonsalves A J *et al* 2011 *Nat. Phys.* **7** 862
[15] Li F *et al* 2013 *Phys. Rev. Lett.* **110** 135002
[16] Rowlands-Rees T P *et al* 2008 *Phys. Rev. Lett.* **100** 105005
[17] McGuffey C *et al* 2010 *Phys. Rev. Lett.* **104** 025004
[18] Pak A *et al* 2010 *Phys. Rev. Lett.* **104** 025003
[19] Clayton C *et al* 2010 *Phys. Rev. Lett.* **105** 105003
[20] Zeng M *et al* 2014 *Phys. Plasmas* **21** 03070
[21] Kamperidis C *et al* 2014 *Plasma Phys. Control. Fusion* **56** 084007
[22] Mirzaie M *et al* 2015 *Sci. Rep.* **5** 14659
[23] Irman A *et al* 2018 *Plasma Phys. Control. Fusion* **60** 044015
[24] Katsouleas S W T *et al* 1987 *Part. Accel.* **22** 81
[25] Tzoufras M *et al* 2008 *Phys. Rev. Lett.* **101** 145002
[26] Rechatin C *et al* 2009 *Phys. Rev. Lett.* **103** 194804
[27] Li S *et al* 2014 *Opt. Express* **22** 29578
[28] Mirzaie M *et al* 2018 *Phys. Plasmas* **25** 043106
[29] Li S *et al* 2018 *Plasma Phys. Control. Fusion* **60** 085020
[30] Ain Q *et al* 2018 *Plasma Phys. Control. Fusion* **60** 085012
[31] Hafz N M *et al* 2007 *Appl. Phys. Lett.* **90** 151501
[32] Hafz N A M *et al* 2010 *Appl. Phys. Express* **3** 076401
[33] Li S *et al* 2014 *J. Appl. Phys.* **116** 043109
[34] Gao K *et al* 2017 *Plasma Sci. Technol.* **19** 015506
[35] Mirzaie M *et al* 2015 *Rev. Sci. Instrum.* **86** 103502
[36] Fonsecax R A *et al* 2002 *Lecture. Notes Comput. Sci.* **2331** 342
[37] Ammosov M V *et al* 1986 *Z. Eksp. Teor. Fiz.* **91** 2008
[38] Bruhwiler D L *et al* 2003 *Phys. Plasmas* **10** 2022
[39] Kalmykov S *et al* 2009 *Phys. Rev. Lett.* **103** 135004
[40] Tsung F S *et al* 2004 *Phys. Rev. Lett.* **93** 185002
[41] Mangles S P D *et al* 2008 *IEEE Trans. Plasma Sci.* **36** 1715
[42] Manahan G G *et al* 2017 *Nat. Commun.* **8** 15705
[43] Hafz N A M *et al* 2016 *High Power Laser Sci. Eng.* **4** e24